Yousuf and Hadi *Chin. J. Mech. Eng.* (2021) 34:24
https://doi.org/10.1186/s10033-021-00533-y

Chinese Journal of Mechanical Engineering

ORIGINAL ARTICLE Open Access

Contact Stress Distribution of a Pear Cam Profile with Roller Follower Mechanism

Louay S. Yousuf[1*] and Nabil Hassan Hadi[2]

Abstract

The problem of this paper is the high contact stress at the point of contact between the cam and the follower. A pear cam and roller follower mechanism were studied and analyzed for different position of the follower and different contact compression load. The objective of this paper is to study the effect of contact compression load on the contact stress distribution of the cam profile at the point of contact. Four different positions of the follower with the cam was considered (0°, 90°, 180°, and 270°). The theory of circular plate was applied to derive the analytic solution of the contact stress. The numerical simulation had been done using ANSYS Ver. 19.2 package to determine the contact stress, while SolidWorks software was used to investigate follower displacement, velocity, and acceleration. Four distinct values of the compression contact load, such as 3.121 N, 6.242 N, 9.364 N, and 12.485 N, were used in the numerical simulation. In the experiment setup, a photo-elastic technique was carried out in the field of polarized light to exhibit the stress distribution on the cam specimen. The annealed PSM-4 backalate material was used in the experiment setup. The experimental value of contact stress was checked and verified analytically and numerically at the point of contact. The innovation in this paper the use of spring-damper system which reduce the value of contact stress at the point of contact. The contact stress was maximum 2.136 MPa when the follower located at 270° with the cam, while the contact stress was minimum 1.802 MPa when the follower located at 180° at compression load 12.485 N.

Keywords: Contact stress, Compression load, Bending deflection, Photo-elastic technique, Finite element analysis

1 Introduction

Cam-follower system is connected to a bionic robotic through a linkage mechanisms to keep the robot walking on a horizontal territory. The contact stress between the cam and the follower is crucial especially at high speed. In this paper, spring-damper system was used at the end of the follower stem to retain the contact stress as much as possible. Pear cam with roller follower mechanism is extensively used in paper processing machines and automatic assembly lines. Sundar et al. [1] used Hertzian contact theory to calculate the contact stiffness at the point of contact. They analyzed numerically the coefficient of restitution. The Hertzian laws were used with a damping term to accommodate the energy loss during the impact [2]. The stiffness model for the active and dwell periods of the globoidal fluctuation due to the contact. They investigated cam was used by Kuang et al. to characterize the mesh stiffness the correlation between the dynamic response of the globoidal cam system and the motor driving speed numerically and experimentally [3]. A cam profile with concave-convex surface of contact had been selected between the cam and follower to suppress the high contact forces at high speeds. Moreover, a hertz contact theory of stress analysis is important to improve the contact fatigue life cycles of cam-follower system. Hua et al. found that the smooth surface of cam profile provides a (53%) reduction in maximum subsurface von Mises stress [4]. Contact stress is reduced to (41%) experimentally by taking into consideration the use of a constant velocity in a dwell stroke [5]. Hsu et al. [6] used a cam mechanism with a translating follower of a dual concave faces to reduce the contact stress over the constant-breadth and the constant-diameter of the cam.

*Correspondence: louaysabah79@yahoo.com
[1] Department of Mechanical Engineering, San Diego State University, 5500 Campanile Drive, San Diego, CA 92182-1323, USA
Full list of author information is available at the end of the article

Fabien et al. [7] selected a cam with dwell-rise-dwell profile to reduce the peak of contact stress over a range of speeds. Angeles et al. [8] calculated the contact pressure into a series of a harmonic waves of a local deformation and sub-surface stress fields. Optimal-control-theory was used by Chew et al. to optimize the contact stress and pressure angle of D-R-D and D-R-R-D cam profiles numerically [9, 10].

The problem of this paper is the high contact stress at the point of contact between the cam and the follower. The contribution of this research is the use of spring-damper system (one degree of freedom system) at the end of the follower stem. The innovation in this paper the use of spring-damper system which reduce the value of contact stress at the point of contact. The aim of this paper is to study the effect of contact compression load on the contact stress distribution of a pear cam profile with roller follower mechanism.

2 Analytic Solution of Dynamic Response

The follower with simple harmonic motion was assumed since it is widely used and simple to design. Cam-follower mechanism was treated as a one-degree-of-freedom system as indicated in Figure 1 [11].

The system with a mass ($m = 0.2759$ kg), spring stiffness ($k = 7$ N/mm), and viscus damper coefficient ($c = 0.875$ N·s/mm) [12] was considered in the solution of one degree of freedom equation. The equation of motion of cam-follower mechanism is as below:

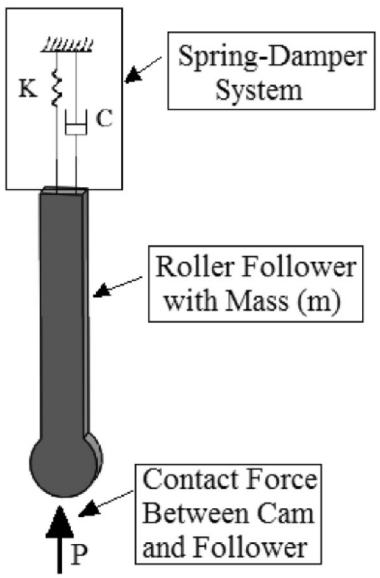

Figure 1 One degree of freedom system

$$\ddot{x} + \frac{cg}{w}\dot{x} + \frac{kg}{w}x = F\sin(\Omega t), \tag{1}$$

where:

$$\frac{cg}{w} = 2\beta, \frac{kg}{w} = \omega^2, F = P\frac{g}{w}.$$

After simplification the equation of motion will be:

$$\ddot{x} + 2\beta\dot{x} + \omega^2 x = F\sin(\Omega t). \tag{2}$$

The homogeneous solution of Eq. (2) is:

$$x_H = e^{-\beta t}\left[C_1\sin\left(\sqrt{\omega^2 - \beta^2}t\right) + C_2\cos\left(\sqrt{\omega^2 - \beta^2}t\right)\right]. \tag{3}$$

The particular solution of Eq. (2) is:

$$x_P = C_3\sin(\Omega t) + C_4\cos(\Omega t), \tag{4}$$

where C_1, C_2, C_3 and C_4 are constants. The first and second derivatives of Eq. (4) are:

$$\dot{x}_P = \Omega C_3\cos(\Omega t) - \Omega C_4\sin(\Omega t),$$

$$\ddot{x}_P = -\Omega^2 C_3\sin(\Omega t) - \Omega^2 C_4\cos(\Omega t).$$

Substitute $x_P, \dot{x}_P, \ddot{x}_P$ into Eq. (2) to obtain:

$$C_3 = \frac{X_{st.}}{H}\left[1 - \left(\frac{\Omega^2}{\omega^2}\right)\right],$$

$$C_4 = -\frac{x_{st.}}{H}\frac{2\beta\Omega}{\omega^2},$$

where

$$x_{st.} = \frac{F}{\omega^2},$$

$$H = [1 - (\frac{\Omega^2}{\omega^2})]^2 + \frac{4\beta^2\Omega^2}{\omega^2}.$$

The complimentary solution is as below:

$$x_C = x_H + x_P. \tag{5}$$

Substitute Eq. (3) and Eq. (4) into Eq. (5) to obtain:

$$x_C = e^{-\beta t}\left[C_1\sin\left(\sqrt{\omega^2 - \beta^2}t\right) + C_2\cos\left(\sqrt{\omega^2 - \beta^2}t\right)\right] + \frac{x_{st.}}{H}\left[1 - \left(\frac{\Omega^2}{\omega^2}\right)\right]\sin(\Omega t) - \frac{x_{st.}}{H}\frac{2\beta\Omega}{\omega^2}\cos(\Omega t). \tag{6}$$

The constants C_1 and C_2 are calculated from the initial boundary conditions as illustrated below:

B.C. (1) at $t = 0, x_C = 0$, B.C. (2) at $t = 0, \dot{x}_C = 0$.

After applying the boundary conditions on Eq. (6), the constants C_1 and C_2 will be:

$$C_1 = \frac{\Omega X_{st.}[\frac{\Omega^2}{\omega^2} + \frac{2\beta^2}{\omega^2} - 1]}{H\sqrt{\omega^2 - \beta^2}},$$

$$C_2 = \frac{2X_{st.}\beta\omega}{H\omega^2}.$$

The general solution of follower response is as below:

$$X_C = e^{-\beta t}\left[\frac{\Omega X_{st.}\left[\frac{\Omega^2}{\omega^2} + \frac{2\beta^2}{\omega^2} - 1\right]}{H\sqrt{\omega^2 - \beta^2}}\sin\left(\sqrt{\omega^2 - \beta^2}t\right) + \frac{2X_{st.}\beta\omega}{H\omega^2}\cos\left(\sqrt{\omega^2 - \beta^2}t\right)\right] + \frac{x_{st.}}{H}\left[1 - \left(\frac{\Omega^2}{\omega^2}\right)\right]\sin(\Omega t) - \frac{x_{st.}}{H}\frac{2\beta\Omega}{\omega^2}\cos(\Omega t). \quad (7)$$

3 Numerical Simulation of Contact Model of Basic Kinematic Relationships

SolidWorks software was used to draw a disc cam, roller follower, and the two guides to investigate follower linear displacement, velocity, and acceleration at the point of contact [13]. Before the cam start spinning, a spring with elastic constants such as spring constant ($k_1 = 38.0611$ N/mm), length ($l = 28$ mm}), spring index ($C_1 = 7$), preload extension ($\Delta = 37$ mm), coil diameter ($d = 0.8$ mm) and outside diameter ($OD = 6.4$ mm) was selected. In this paper, the spring force was expressed as an external force in SolidWorks software to keep the cam and follower in permanent contact. The spring force was applied at the point in which it has the coordinates (x: 0, y: 161.76 mm, z: 0) between the follower body and the installation table. The contact expression force function was as below [14]:

$$P = k_1(\Delta + x(t)) - kx(t) - c\dot{x}(t) - \frac{w}{g}\ddot{x}(t). \quad (8)$$

The spring and damper were applied at the end point of the follower stem in which it has the coordinates (x: 0, y: 227.79 mm, z: 0). The contact model of a pear cam and roller follower with its dimensions is illustrated in Figure 2.

The area of contact can be assumed to be semi-ellipsoid in SolidWorks software with a rectangular contact zone of a half-width (b) and length (L) (contact between two parallel cylinders), as below [15]:

$$b_1 = K_b\sqrt{P}, \quad (9)$$

where

$$K_b = \sqrt{(\frac{2}{\pi L})\frac{\frac{1-\nu_1^2}{E_1} + \frac{1-\nu_2^2}{E_2}}{\left(\frac{1}{d_1}\right) + \left(\frac{1}{d_2}\right)}}.$$

The maximum depth (z_1) underneath the surface of contact in terms of damping ratio was occurred when ($z_1/b = 0.786$) as illustrated in the following equation [15, 16]:

$$\zeta = \frac{z}{b_1}. \quad (10)$$

The penetration distance (δ) is related to the field surface displacement when ($\nu_1 = \nu_2 = \nu$) and ($E_1 = E_2$) which characterized by the following equation [17]:

$$\delta = \frac{2P(1-\nu^2)}{\pi LE}\left[\frac{2}{3} + \ln\frac{4R_1}{b} + \ln\frac{4R_2}{b}\right], \quad (11)$$

where

$$\frac{1}{E} = \frac{1-\nu_1^2}{E_1} + \frac{1-\nu_2^2}{E_2}.$$

The impact between the follower and the cam had been occurred due to the impulse and momentum theory of the follower velocity:

$$V_C = \sqrt{2g\Delta h}. \quad (12)$$

Hertzian contact theory predicts the value of the exponent (n) based on the flattening law of the shape of the

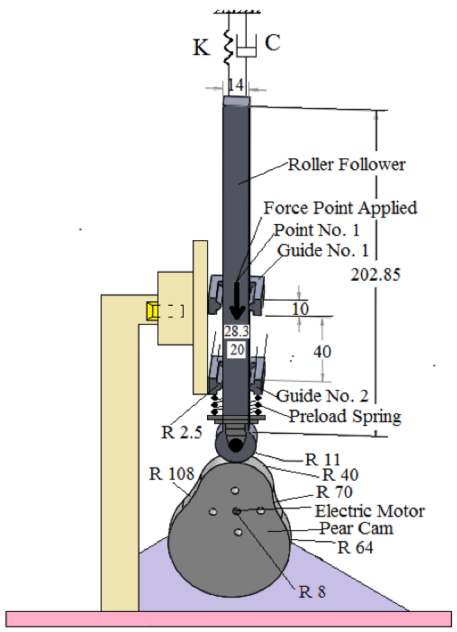

Figure 2 Contact model of cam-follower system

first asperity. The exponent value (n) is ranging from 1.5 for spherical punch to 2 for wedge shaped punch [15, 18].

The contact parameters, such as the contact force (P), contact bodies stiffness (K_b), damping ratio (ζ), penetration (δ), sliding contact velocity (V_C), and exponent (n), were entered as an inputs in SolidWorks software to calculate follower linear displacement.

4 Cam Profile Layout

The points of cam profile were calculated by rotating the radius of curvature of the roller follower in an opposite direction to the rotation of the cam [19]. The parameters ($\rho(\theta), S(\psi), \psi$ and θ) were used in the equation of cam profile as follows [20]:

$$x_1 = e\cos(\psi) + S(\psi)\sin(\psi), \tag{13}$$

$$y_1 = -e\sin(\psi) + S(\psi)\cos(\psi), \tag{14}$$

Where

$$e = \rho(\theta)\cos(\psi + \theta),$$

$$S(\psi) = \rho(\theta)\sin(\psi + \theta).$$

The points of cam profile were calculated using Eq. (15) and Eq. (16):

$$x_{C1}(\psi) = e\cos\left(\psi + a_1\right) + S(\psi)\sin(\psi + a_1), \tag{15}$$

$$y_{C1}(\psi) = -e\sin\left(\psi + a_1\right) + S(\psi)\cos(\psi + a_1). \tag{16}$$

Figure 3 shows the verification design of analytic and numerical cam profile. The numerical cam profile was drawn using SolidWorks software. The analytic cam profile was designed by applying Eq. (15) and Eq. (16) at the point of contact between the cam and the follower.

There was no error at the base circle of the cam because the contact between the cam and the follower when ($a_1 = 85°$). The analytic solution of Eq. (15) and Eq. (16) gives the exact value of Cartesian coordinates of the cam profile at the point of contact with no error. The tangent command in SolidWorks software was used between flank No. (1) and the nose or between flank No. (2) and the nose which gives an error to the Cartesian coordinate during the drawing. The error between the analytic solution and SolidWorks software is around (8.823%).

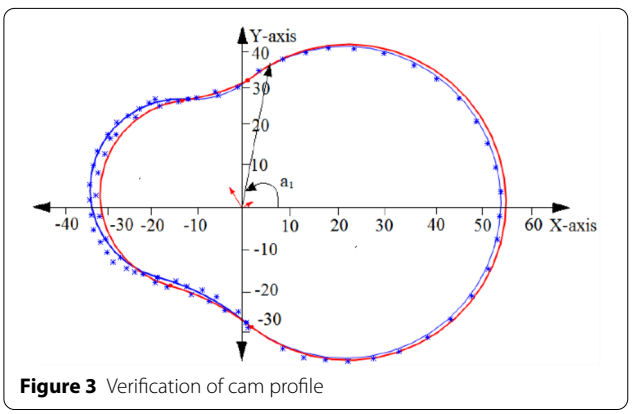

Figure 3 Verification of cam profile

5 Follower Motion Verification

A pear cam with return-rise-dwell-return-rise-dwell-return profile was proposed. The cam starts spinning with a return stroke for (20°) followed by a rise stroke with (80°) and a dwell motion for the next (8°). Return stroke for the next (67°) of the cam rotation had been occurred accompanied by a rise stroke with (101°) and a dwell motion for the next (7°) followed by return stroke for the next (77°) of the cam cycle. Follower displacement was determined using Eq. (7), while the numerical simulation of follower displacement was done using SolidWorks software. Figure 4 indicates the verification of follower displacement.

6 Numerical Simulation of Contact Stress

The numerical simulation of bending deflection was done by using ANSYS Ver. 19.2 package [21]. Linear elastic isotropic model was used to calculate the bending deflection of the cam profile. Element (PLANE 42) was assigned to create the mesh generation of finite element analysis. This element was defined by four nodes which is having two degrees of freedom at each node:

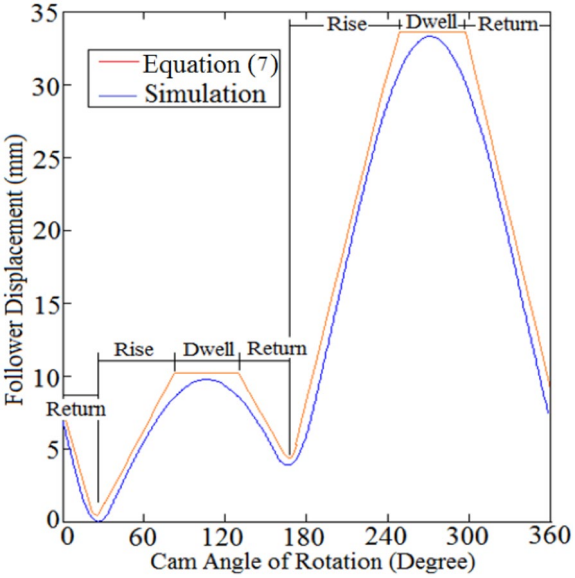

Figure 4 Verification of follower displacement

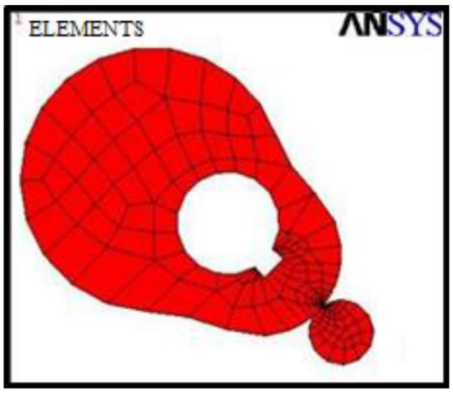

Figure 5 Mesh generation when the follower located at 0° with the cam

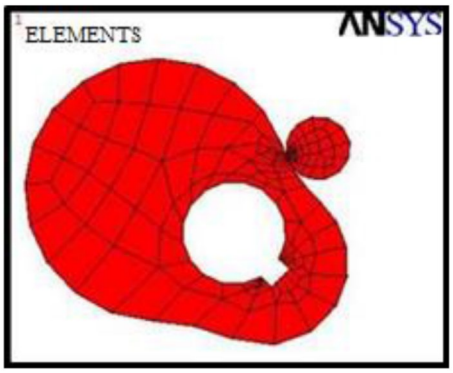

Figure 6 Mesh generation when the follower located at 90° with the cam

(translations in the nodal x, y directions). The translation degrees of freedom were assumed to be zero (clamped boundary conditions) at the hub radius when ($r = r_1$) of the motor shaft. In contact analysis, element (TARGE 170) and element (CONTA 174) had been used to create the contact mesh generation between the target and the contact surfaces. The disc cam represented the source, while the roller follower was the target. In this simulation, two load steps were used. In the first load step, a small displacement was imposed on the target surface because of the small value of the radius of curvature. In the second load step, the small imposed displacement was deleted in which the force was applied at the point of contact. Four different values of compression loads, such as 3.121 N, 6.242 N, 9.364 N, and 12.485 N, were considered in the simulation. The follower was located at 0°, 90°, 180°, and 270° with the cam. Figures 5, 6, 7, 8 show the mesh generation of the cam with the follower at the point of contact.

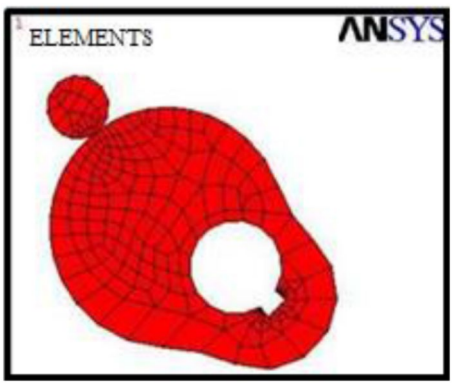

Figure 7 Mesh generation when the follower located at 180° with the cam

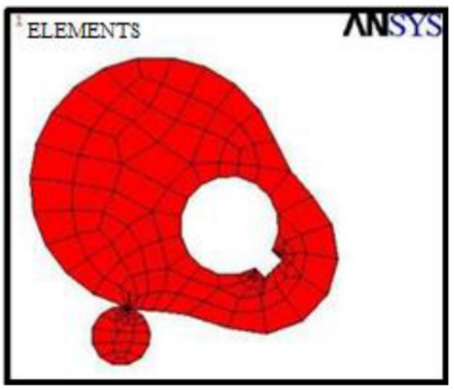

Figure 8 Mesh generation when the follower located at 270° with the cam

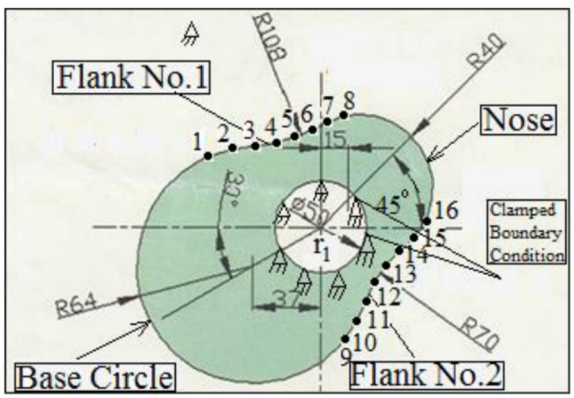

Figure 9 Points of the cam profile

In this study, the profile of disc cam was divided into two tracks at the point of contact:

Path No. (1): [nose, flank (1), and base circle].

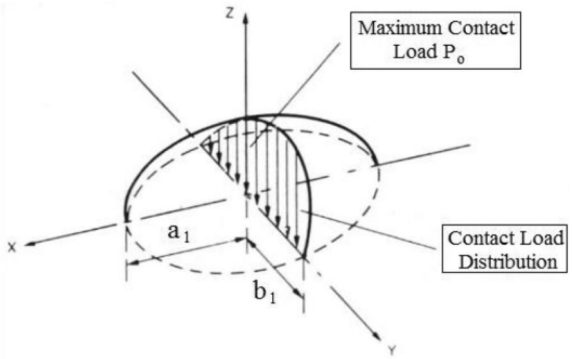

Figure 10 Contact load distribution between two curved bodies [24]

Path No. (2): [nose, flank (2), and base circle].

Path No. (1) was formed from the points 1, 2, 3, 4, 5, 6, 7, 8, while path No. (2) was arranged from the points 9, 10, 11, 12, 13, 14, 15, 16, as shown in Figure 9.

7 Contact Load Calculation

Both cam and roller follower were assumed to be parallel cylinders with the length of ($L = 10$ mm) in the calculation of contact load. A convex surface of the cam profile was considered to have positive radius of curvature, while the concave surface was negative [22]. In this paper, the contact pressure showed that the intensity of the pressure between the two contacting surfaces could be represented by the elliptical or semi-ellipsoid regions as indicated in Figure 10, [23]. Therefore, this small region exhibits a very high contact stress specifically during the active region of the cam, when the most significant loading of the followers occurs [5].

The maximum contact load is given by the volume of a small elliptical region (contact between two curved surfaces) as below [24]:

$$P_o = \frac{3P}{2\pi a_1 b_1}, \tag{17}$$

where

$$a_1 = m_1\left(\frac{3P\Delta_1}{4A_1}\right)^{1/3},$$

$$b_1 = n_1\left(\frac{3P\Delta_1}{4A_1}\right)^{1/3},$$

$$A_1 = 0.5\left[\frac{1}{R_1} + \frac{1}{R_1'} + \frac{1}{R_2} + \frac{1}{R_2'}\right],$$

$$B_1 = 0.5[\left(\frac{1}{R_1} - \frac{1}{R_1'}\right)^2 + \left(\frac{1}{R_2} - \frac{1}{R_2'}\right)^2 + 2(\frac{1}{R_1} - \frac{1}{R_1'})(\frac{1}{R_2} - \frac{1}{R_2'})\cos(2\Psi_1)]^{0.5},$$

$$\Delta_1 = \frac{1}{E_1}\left(1 - \nu_1^2\right) + \frac{1}{E_2}\left(1 - \nu_2^2\right),$$

$$\psi_1 = \tan^{-1}\left(\frac{\dot{x}(t)}{x(t) + R_b}\right).$$

The values of (m_1) and (n_1) were taken from Table 1 based on the pressure angle between the cam and the follower [24]:

$$\alpha = \cos^{-1}\left(\frac{B_1}{A_1}\right).$$

8 Experiment Setup of Photo-Elastic Technique

The experimental setup was carried out using a photo-elastic technique [25, 26]. Four different positions of the follower with the cam were considered (0°, 90°, 180°, and 270°) by taking into consideration four distinct value of contact compression load, such as 3.121 N, 6.242 N, 9.364 N, and 12.485 N. A photo-elastic stress analysis is one of the most powerful techniques in which it gives an overall picture for the stress field quickly. Photo-elastic approach deals with the systems which is having complicated geometry, such as (pear cam), complicated loading conditions or both. Photo-elastic rig is constructed from a plane polariscope with a light source, a polarizer, the specimen, and an analyzer that is always crossed with respect to the polarizer, as indicated in Figure 11. Plane polariscope with a dark field was used to show the regions of stress intensification.

In this paper, the zero degree direction of polarization was assumed to be vertical in which it rotates the polarizer and analyzer together in order to determine the principal stress directions. Pear cam and roller follower were made from an annealed plastic of PSM-4 backalate material with modulus of elasticity (4 MPa.) and Poisson's ratio (0.5). Machining process was used during the manufacturing of the cam and the follower in which a

Table 1 Values of (m_1&n_1) versus the angle of contact (α°) [24]

α (°)	20	40	60	80	90
m_1	3.778	2.136	1.486	1.128	1
n_1	0.408	0.567	0.117	0.893	1

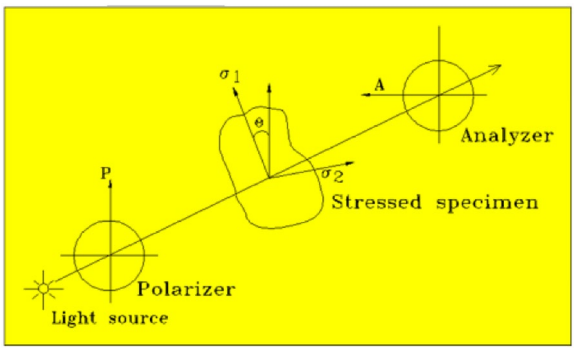

Figure 11 Plane polariscope of photo-elasticity apparatus

smooth surfaces were created and left no residual stress on the model. The PSM-4 specimen was placed in the trough to remove the cracks caused by machining and after machining, the specimen was placed in the polariscope to ensure that there is no residual stress occurred. The follower axis passed longitudinally through the axis of pear cam when the follower located at 0° and 180° degrees and transversely through the axis of pear cam when the follower located at 90° and 270°. In this paper, photo-elasticity technique had been applied over two stages. In the first stage, a material calibration was performed using four-point bending test in order to calculate the stress fringe constant. In the second stage, a sequence of colored brands was implemented based on a birefringence phenomenon of the pear cam geometry. Four-point bending test was used effectively to extract the value of stress fringe constant. The straight beam was supported by two ends, while a transverse downward loading had been applied at the two points as illustrated in Figure 12a. A sample of straight beam of four-point bending test was manufactured using ASTM (D6272) dimensions, as indicated in Figure 12b.

The value of stress fringe constant (f_σ) can be determined experimentally by inducing a difference between σ_1 and σ_2 in a model that is made from PSM-4 material, as in below:

$$f_\sigma = h\frac{(\sigma_1 - \sigma_2)}{N}, \tag{18}$$

$$\sigma_1 - \sigma_2 = \frac{My}{I} = \frac{F_s(L_o - L_1)y}{4I}. \tag{19}$$

By substituting Eq. (18) into Eq. (17) and after simplification we can obtain the value of quantity (Z), as in below:

$$Z = \frac{F_s(L_o - L_1)yh}{4I}, \tag{20}$$

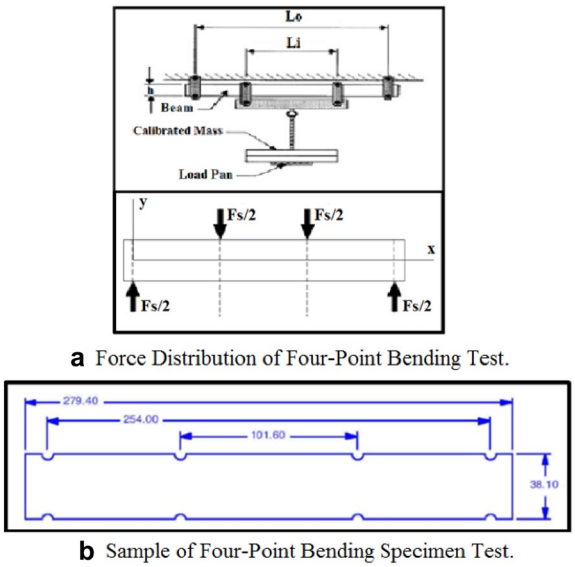

a Force Distribution of Four-Point Bending Test.

b Sample of Four-Point Bending Specimen Test.

Figure 12 Visualization of forces and ASTM dimensions in a straight beam subjected to four-point bending test

where

$$F_s = m_1 g, y = \frac{w}{2}, I = \frac{hw^3}{12},$$
$$m_1 = 0.318\ \text{kg}, 0.636\ \text{kg}, 0.954\text{kg}, 1.272\ \text{kg}.$$

Hence, (f_σ) can be determined by plotting the quantity (Z) versus the fringe order (N), as shown in Figure 13 in which the stress fringe constant represents the slope.

From Figure 13, it can be found that the value of stress fringe constant is ($f_\sigma = 178.323\frac{N}{m.\,\text{fringe}}$). The mass with the value ($m_1 = 1.272\,\text{kg}$) was used in the experiment

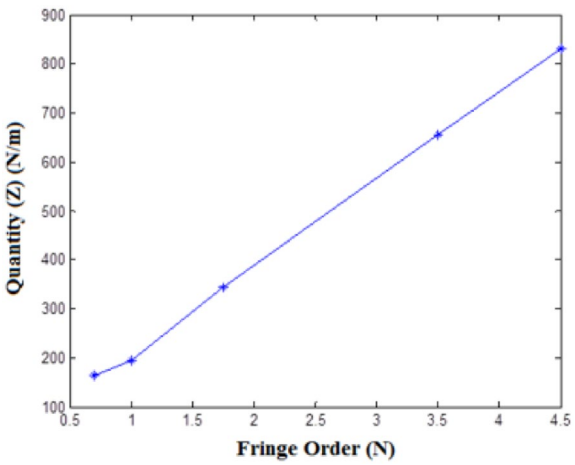

Figure 13 Calibration of fringe constant (f_σ)

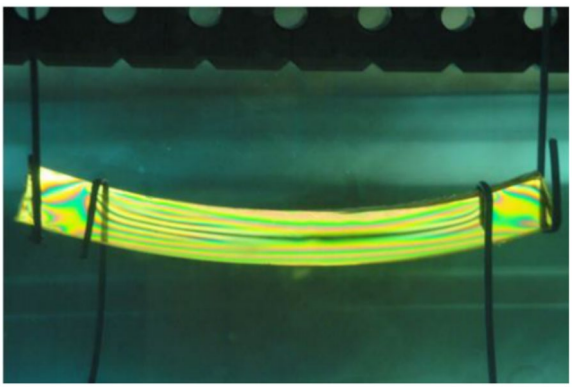

Figure 14 Four-point bending test using photo-elastic technique

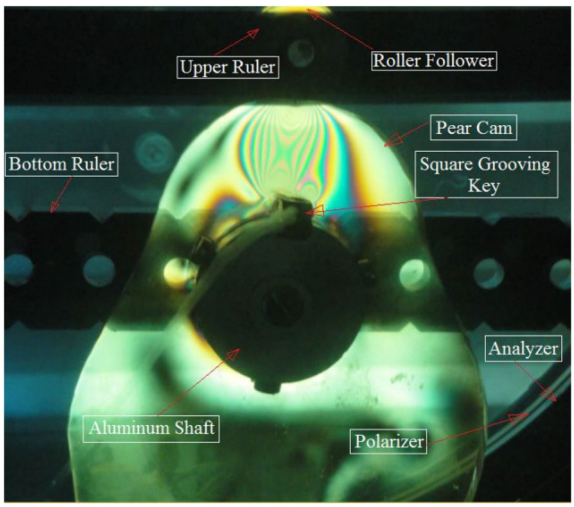

Figure 15 Stress analysis when the follower located at 0° with the cam

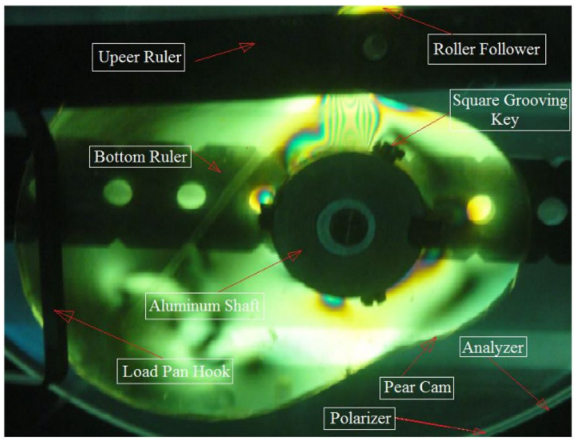

Figure 16 Stress analysis when the follower located at 90° with the cam

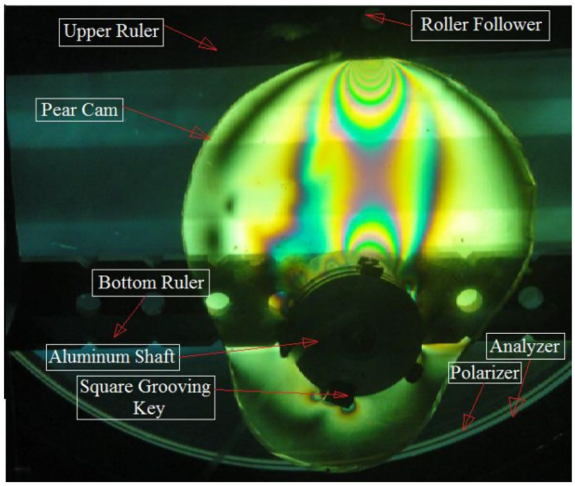

Figure 17 Stress analysis when the follower located at 180° with the cam

since the fringe order (N) was more obvious and clear. The photo-elasticity experiment of four-point bending test is shown in Figure 14.

Figures 15, 16, 17, 18 reflect the stress distribution for different positions of the follower (0°, 90°, 180°, and 270°) with the cam using photo-elastic technique.

In this paper, photo-elastic technique represents the three dimensional of experimental stress analysis in two dimensional form using the state of plane stress. The pear cam with the hub diameter (25 mm) was mounted on the aluminum shaft, while the aluminum shaft with the hub diameter (6 mm) was installed on the square grooving key. The sample test of pear cam and roller follower were cut off from a 6.35 mm thick plate of PSM-4 material. The pear cam and the aluminum shaft were suspended on the bottom ruler, while the roller follower with the diameter (5 mm) was installed on the upper ruler to make the contact between the cam and the follower. The upper and bottom rulers were suspended on the photo-elastic apparatus. The weights was hanged on a hook load pan to exhibit the stress analysis in the field of polarized light in order to represent the birefringence phenomenon of the pear cam geometry.

9 Analytic Solution of Contact Stress Analysis

The general equation of circular plate in terms of (r, Θ, t) is [27]:

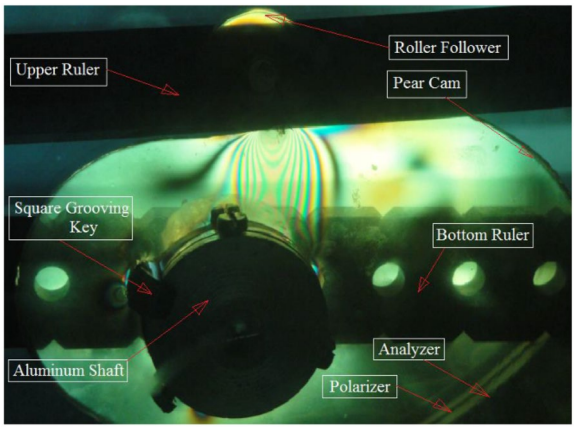

Figure 18 Stress analysis when the follower located at 270° with the cam

$$\left(\frac{\partial^2}{\partial r^2}+\frac{2}{r}\right)M_r-\left(\frac{1}{r}\frac{\partial}{\partial r}-\frac{1}{r^2}\frac{\partial^2}{\partial\theta^2}\right)M_\theta-\left(\frac{2}{r}\frac{\partial^2}{\partial r\partial\theta}+\frac{2}{r^2}\frac{\partial}{\partial\theta}\right)M_{r\theta}+\rho\frac{\partial^2 W}{\partial t^2}+P_o=0, \tag{21}$$

where

$$M_r=-D\left[\frac{\partial^2 W}{\partial r^2}+\nu_1\left(\frac{1}{r}\frac{\partial W}{\partial r}+\frac{1}{r^2}\frac{\partial^2 W}{\partial\theta^2}\right)\right],$$

$$M_\theta=-D\left[\left(\frac{1}{r}\frac{\partial W}{\partial r}+\frac{1}{r^2}\frac{\partial^2 W}{\partial\theta^2}\right)+\nu_1\frac{\partial^2 W}{\partial r^2}\right],$$

$$M_{r\theta}=-D(1-\nu_1)\left[\frac{1}{r}\frac{\partial^2 \mathrm{W}}{\partial r\partial\theta}-\frac{1}{r^2}\frac{\partial W}{\partial\theta}\right],$$

$$D=\frac{E_1h^3}{12(1-\nu_1^2)}.$$

Substitute M_r, M_θ, and $M_{r\theta}$ into Eq. (21), it can be obtained [27]:

$$\frac{\partial^4 W}{\partial r^4}+\frac{2}{r}\frac{\partial^3 W}{\partial r^3}-\frac{1}{r^2}\frac{\partial^2 W}{\partial r^2}+\frac{1}{r^3}\frac{\partial W}{\partial r}+\frac{2}{r^2}\frac{\partial^4 W}{\partial r^2\partial\theta^2}-\frac{2}{r^3}\frac{\partial^3 W}{\partial r\partial\theta^2}+\frac{4}{r^4}\frac{\partial^2 W}{\partial\theta^2}+\frac{1}{r^4}\frac{\partial^4 W}{\partial\theta^4}+\frac{\rho}{D}\frac{\partial^2 W}{\partial t^2}=\frac{P_o}{D}. \tag{22}$$

The homogeneous solution of Eq. (22) will be [28]:

$$W(r,\theta,t)_H=\sum_{m=1,3,5}^{\infty}[A\sin(m\theta)+B\cos(m\theta)]\sin(\omega_n t), \tag{23}$$

where

$$A=A_m r^m+B_m r^{-m}+C_m r^{m+2}+D_m r^{m-2},$$

$$B=A'_m r^m+B'_m r^{-m}+C'_m r^{m+2}+D'_m r^{m-2}.$$

For non-symmetric cam profile, the deflection, slope, and the moment must be infinite at the center of the plate. Then the homogeneous solution of Eq. (22) will be [28]:

$$W(r,\theta,t)_H=\sum_{m=1,3,5}^{\infty}[(A_m r^m+C_m r^{m+2})\sin(m\theta)+(A'_m r^m+C'_m r^{m+2})\cos(m\theta)]\sin(\omega_n t). \tag{24}$$

By applying the infinite series theorem on the homogeneous solution of Eq. (24), as in below:

$$r^m\sin(m\theta)=\left(1+r+r^2+r^3+r^4+r^5+\ldots\right)\left(m\theta-\frac{(m\theta)^3}{3!}+\frac{(m\theta)^5}{5!}-\ldots\right).$$

Cam profile was unsymmetrical (odd function), the symmetric terms (even function) was ignored, as in follows:

$$r^m\sin(m\theta)=(rm\theta)-\frac{(rm\theta)^3}{3!}+\frac{(rm\theta)^5}{5!}=\sin(rm\theta)$$

Also the same procedure was processed on the second term:

$$r^{m+2}\sin(m\theta)=\sin(r\theta).$$

As stated above:

$$r^m\cos(m\theta)=\left(1+r+r^2+r^3+r^4+\ldots\right)\left(1-\frac{(m\theta)^2}{2!}+\frac{(m\theta)^4}{4!}-\ldots\right)=\cos(r\theta),$$

$$r^{m+2}\cos(m\theta)=\cos(r\theta).$$

The homogeneous solution of Eq. (22) will be [28]:

$$W(r,\theta,t)=[A\sin(r\theta)+B\cos(r\theta)]\sin(\omega_n t), \tag{25}$$

where A and B are constants.

The particular solution of Eq. (22) will be [28]:

$$W(r,\theta,t)_P = \sum_{m=1,3,5}^{\infty} [Cr^4 \sin(m\theta)]\sin(\Omega t), \tag{26}$$

where C is constant of the particular solution.

By applying the infinite series theorem on the particular solution, as indicated below:

$$r^4\sin(m\theta) = \left(1 + r + r^2 + r^3 + r^4 + \dots\right)\left(m\theta - \frac{(m\theta)^3}{3!} + \frac{(m\theta)^5}{5!}\right).$$

By ignoring the higher order terms of the above series and by taking the non-symmetric terms into account:

$$r^4\sin(m\theta) = rm\theta.$$

The particular solution of Eq. (22) will become:

$$W(r,\theta,t)_P = Cr\theta\sin(\Omega t) \tag{27}$$

Substitute Eq. (27) into Eq. (22), the particular solution of Eq. (22) will be:

$$W(r,\theta,t)_P = \left[\frac{P_o R_P^3}{\theta_P D} + \frac{\rho\Omega^2 R_P^3}{\theta_P D}\right] r\theta\sin(\Omega t). \tag{28}$$

The general solution of bending deflection of the cam profile of Eq. (22) will be depicted in the following equation:

$$W(r,\theta,t) = [A\sin(r\theta) + B\cos(r\theta)]\sin(\omega_n t) + \left[\frac{P_o R_P^3}{\theta_P D} + \frac{\rho\Omega^2 R_P^3}{\theta_P D}\right] r\theta\sin(\Omega t). \tag{29}$$

It can be applied the boundary condition on Eq. (29) to obtain the constants (A) and (B).

(1) At $(r = r_1), (\theta = \theta_P), (t = t_1), W(r,\theta,t) = 0$
(2) At $(r = r_1), (\theta = \theta_P), (t = t_1), \frac{\partial W(r,\theta,t)}{\partial r} = 0.$

The constants A and B is as follows:

$$A = -\left(\frac{P_o R_P^3}{\theta_P D} + \frac{\rho\Omega^2 R_P^3}{\theta_P D}\right)(r_1\theta_P\sin(r_1\theta_P) + \cos(r_1\theta_P))\frac{\sin(\Omega t_1)}{\sin(\omega_n t_1)},$$

$$B = \left(\frac{P_o R_P^3}{\theta_P D} + \frac{\rho\Omega^2 R_P^3}{\theta_P D}\right)(\sin(r_1\theta_P) - \theta_P\cos(r_1\theta_P))\frac{\sin(\Omega t_1)}{\sin(\omega_n t_1)}.$$

The general solution of the bending deflection of the cam profile at the point of contact will become:

Table 2 Verification of contact stress at different compression load and different followers' positions

Load (N)	Location (°)	Experiment	Simulation	Error (%)
3.121	0	0.1544	0.1527	1.101
	90	0.1474	0.1570	6.114
	180	0.0561	0.0593	5.396
	270	0.198	0.2189	9.547
6.242	0	0.2808	0.3054	8.055
	90	0.287	0.3141	8.627
	180	0.1075	0.1186	9.359
	270	0.413	0.4378	5.664
9.364	0	0.4212	0.4581	8.055
	90	0.4352	0.4712	7.640
	180	0.1685	0.1780	5.337
	270	0.6016	0.6569	8.418
12.48	0	0.5876	0.6108	3.798
	90	0.5816	0.6282	7.418
	180	0.2206	0.2373	7.037
	270	0.833	0.8758	4.887

$$W(r,\theta,t) = -\left(\frac{P_o R_P^3}{\theta_P D} + \frac{\rho\Omega^2 R_P^3}{\theta_P D}\right)\frac{\sin(\Omega t_1)}{\sin(\omega_n t_1)} [(r_1\theta_P\sin(r_1\theta_P) + \cos(r_1\theta_P))\sin(r\theta) + (\theta_P\cos(r_1\theta_P) - \sin(r_1\theta_P)) \cos(r\theta)]\sin(\omega_n t) + [\frac{P_o R_P^3}{\theta_P D} + \frac{\rho\Omega^2 R_P^3}{\theta_P D}]r\theta\sin(\Omega t), \tag{30}$$

where $t_1 = \frac{\theta_P}{\Omega}$

The bending deflection of Eq. (30) can be derived once and twice to obtain the contact stress at the point of contact, as in below [29]:

$$M_r = \int_{-\frac{h}{2}}^{\frac{h}{2}} \sigma_r z \, dz, \tag{31a}$$

$$M_\theta = \int_{-\frac{h}{2}}^{\frac{h}{2}} \sigma_\theta z \, dz, \tag{31b}$$

$$M_{r\theta} = \int_{-\frac{h}{2}}^{\frac{h}{2}} \sigma_{r\theta} z \, dz. \tag{31c}$$

After integration, ($\sigma_r, \sigma_\theta,$ and $\sigma_{r\theta}$) will be:

$$\sigma_r = \frac{6M_r}{h^2} \tag{32a}$$

$$\sigma_\theta = \frac{6M_\theta}{h^2} \tag{32b}$$

$$\sigma_{r\theta} = \frac{6M_{r\theta}}{h^2}. \tag{32c}$$

The principal stresses are:

$$\sigma_1 = \frac{\sigma_r - \sigma_\theta}{2} + \sqrt{\left(\frac{\sigma_r + \sigma_\theta}{2}\right)^2 + \sigma_{r\theta}^2}, \tag{33a}$$

$$\sigma_2 = \frac{\sigma_r - \sigma_\theta}{2} - \sqrt{\left(\frac{\sigma_r + \sigma_\theta}{2}\right)^2 + \sigma_{r\theta}^2}. \tag{33b}$$

The general von Mises stress equation is illustrated in the following equation:

$$\sigma_V^2 = \frac{1}{2}\left[(\sigma_1 - \sigma_2)^2 + (\sigma_1)^2 + (\sigma_2)^2\right]. \tag{34}$$

The single trigonometric (m) has been taken as a n infinite series ($m = 1, 2, 3,..., \infty$) in which there will be a compatible between the analytic and numerical solutions. The percentage of error will be under (10%).

10 Results and Discussions

Table 2 shows the experimental and simulation verification of contact stress at different compression load and different followers' positions with the cam profile. The contact stress is increased with the increasing of compression load for all followers' positions with the cam. All values of the contact stress were in MPa.

Figures 19 and 20 show the bending deflection of path of contact No. (1) and No. (2) versus the angle of contact at different values of compression load. The bending deflection is increased with the increasing of compression loads since it reaches the maximum value at points 4 and 12 on flank No. (1) and flank No. (2) respectively. The maximum value of bending deflection is in the middle points of flank No. (1) (0.00157 m) and flank No. (2) (0.00137 m) at compression load (12.485 N). The bending deflection of path No. (1) is higher than path No. (2) because of the bigness of radius of curvature of path No. (1). ANSYS software was used to find the bending deflection of the points on flanks No. (1) and flank No. (2).

Figures 21, 22, 23, 24 show the Von Mises contact stress contour when the follower located at 0°, 90°, 180°, and 270° with the cam at compression load 12.485 N. The contours of contact stresses were determine by using ANSYS software. All values of the contact stress are in MPa. Maximum contact stress is 0.8758 MPa when the follower located at 270° with the cam, while the minimum contact stress is 0.2373 MPa when the follower located at 180°. The contact stress has a minimum value for all compression loads when the follower located at 180° with the base circle of the cam profile since the acceleration fluctuation was equal to zero.

Figure 25 shows the verification of contact stress versus the compression load at different followers' positions with the cam. The analytic results was done using Eq. (34) of Von Mises stress, while the simulation results were done using ANSYS software. In general, the analytic results were very close to ANSYS results within the percentage of error. The percentage of error between the two

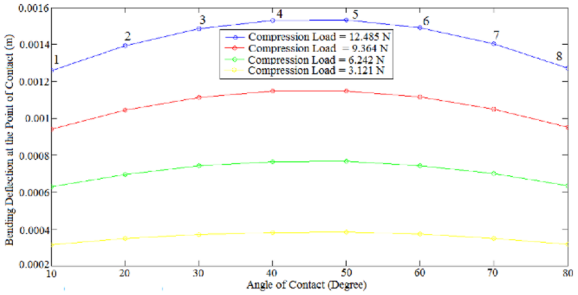

Figure 19 bending deflection against the contact angle of path No. (1)

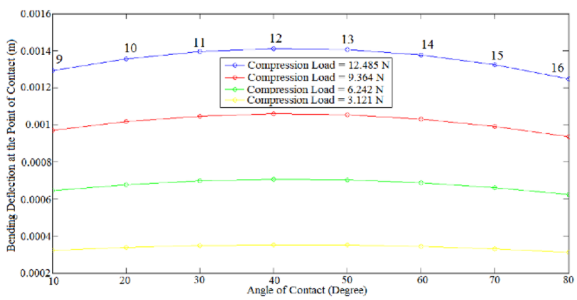

Figure 20 Bending deflection against the contact angle of path No. (2)

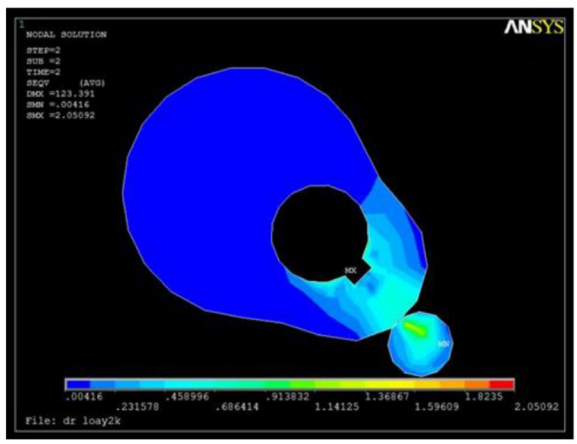

Figure 21 Contact stress contour when the follower located at 0° with the cam

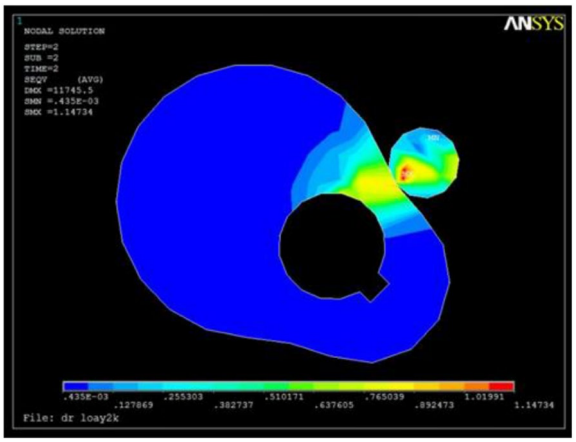

Figure 22 Contact stress contour when the follower located at 90° with the cam

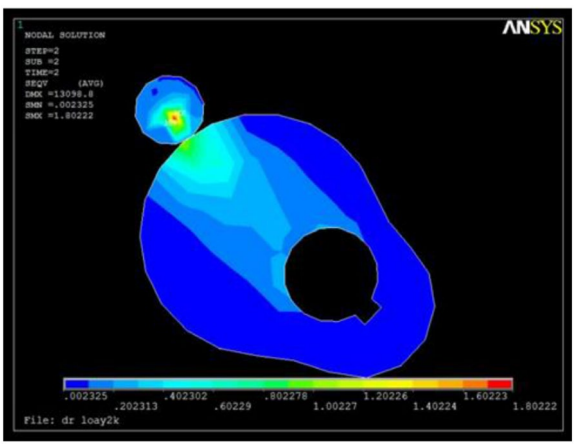

Figure 23 Contact stress contour when the follower located at 180° with the cam

sets of results are acceptable since the results are under 10% at 0°, 90°, 180°, and 270°, respectively.

Figure 26 shows the variation of contact stress with the compression load at different followers' positions 0°, 90°, 180°, and 270° with the cam. The contact stress is increased linearly with the increasing of compression load. The contact stress is maximum when the follower located at 270° with the cam, while the contact stress is minimum when the follower located at 180° with the cam at compression load 12.485 N.

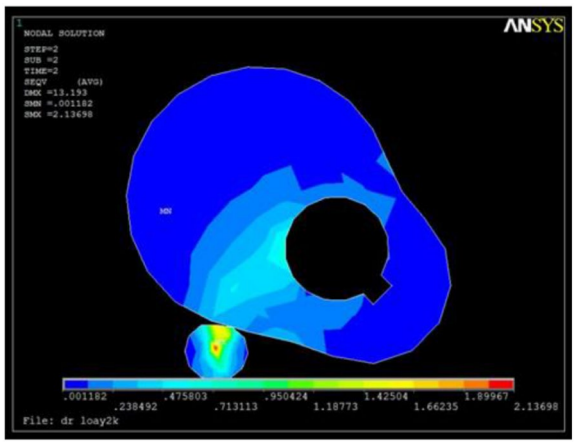

Figure 24 Contact stress contour when the follower located at 270° with the cam

11 Conclusions and Future Work

This study analyzed and discussed the calculation of contact stress distribution at the point of contact for path No. (1) and path No. (2). The numerical procedure was done using ANSYS package and SolidWorks software. SolidWorks software was used to calculate follower displacement, velocity, and acceleration, while ANSYS package was carried out to determine the contact stress. The theory of circular plate was applied to derive the general equation of the bending deflection and contact stress distributions. In the experiment setup, four points bending test and birefringence analysis were conducted using photo-elastic technique to determine the contact stress. The contact stress was maximum 2.136 MPa when the follower located at 270° with the cam, while the contact stress was minimum 1.802 MPa when the follower located at 180° at compression load 12.485 N. The contact stress has a minimum value for all compression loads when the follower located at 180° with the base circle of the cam profile.

The recommendation of the future work is as below:

(1) Contact stress reduction using genetic algorithm technique.
(2) Study the effect of Hertzian contact stress on the bending deflection of cam profile.

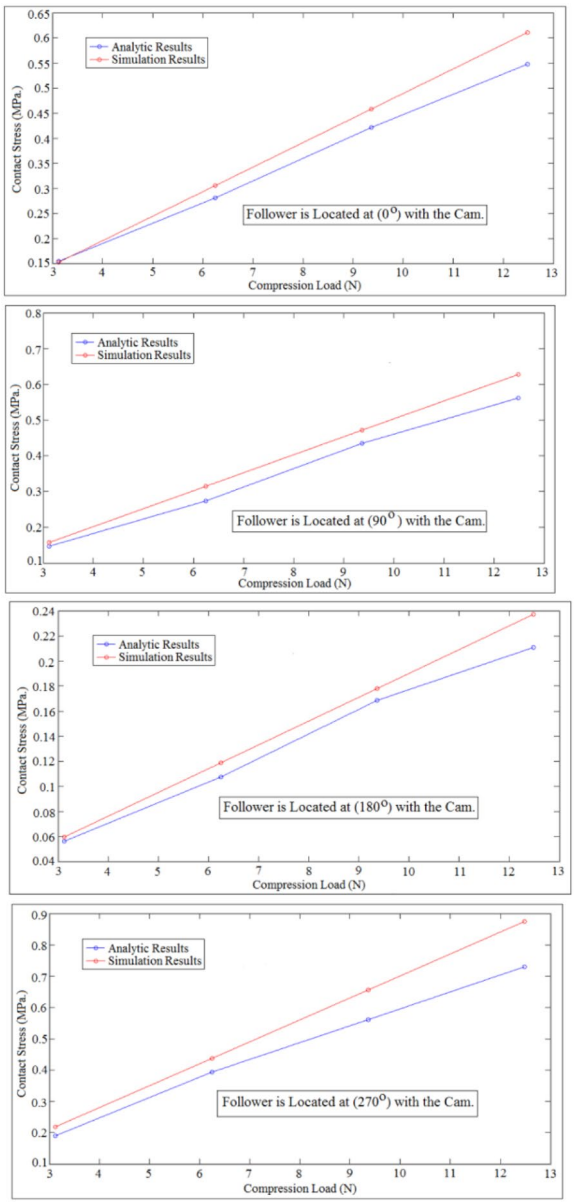

Figure 25 Verification of contact stress when the follower located at 0° and 90°, 180°, and 270° with the cam profile

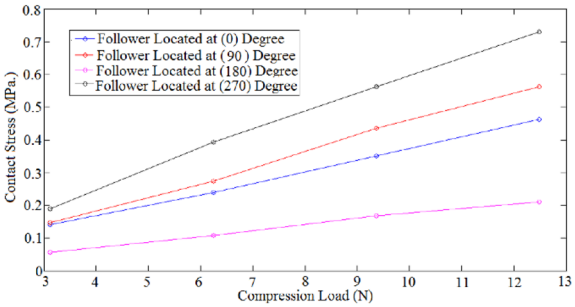

Figure 26 Contact stress is varying with compression load at different locations of the roller follower

Abbreviations

P: Contact force between cam and follower, N; *x*, $\dot{x}, \ddot{x}$: Linear displacement, velocity, and acceleration of the roller follower, mm, mm/s, mm/s^2; *w*: Weight of roller follower, N; *m*: Mass of follower stem, kg; *g*: Gravitational acceleration, mm/s^2; *k*, *c*: Spring stiffness and viscous damping coefficient, N/mm, N·s/mm; x_H, x_P: Homogeneous and particular solutions of the follower displacement, mm; x_C: Analytic complementary solution of the follower displacement, mm; x_{st}: Static deflection, mm; Ω: Cam angular velocity, rad/s; *t*: Time of contact including the time of the dwell stroke, s; Δ: Spring extension due to the preload external force, mm; k_1: Stiffness of the preload spring, N/mm; *L*: Length of the cam and follower along *z*-axis, mm; *b*: Half width of the rectangular contact zone, mm; K_b: Contact body stiffness, N/mm; ν_1, ν_2: Poisson's ratio for cam and follower respectively; E_1, E_2: Modulus of elasticity for both cam and follower respectively, N/mm^2; d_1, d_2: Diameter for cam and follower respectively at the point of contact, mm; z_1: Maximum depth underneath the surface of contact, mm; ζ: Damping ratio; δ: Penetration, mm; R_1, R_2: Diameter for cam and follower respectively at the point of contact, mm; *E*: Equivalent modulus of elasticity, N/mm^2; V_C: Sliding impact velocity, mm/s; Δ*h*: Change in rebounding heights, mm; *n*: Exponent; Ψ: Cam angle, (°); Θ: Angle of contact, (°); ρ(Θ): Radius of curvature at the point of contact, mm; *S*(Ψ): Follower displacement at the point of contact, mm; a_1: Beginning angle of rotation of the dwell stroke, (°); x_{C1}, y_{C1}: Cartesian coordinates of the cam profile at the point of contact, mm; f_σ: Stress fringe constant, N/mm fringe; *N*: Fringe order; F_s: Shear force, N; L_1: Distance between the two ends of the load pan hook, mm; L_o: Distance between the two ends support, mm; *h*: Thickness of PSM-4 material, mm; *W*: Width of PSM-4 material, mm; *I*: Second moment of inertia, mm^4; m_1: Mass of the grooved disc in the load pan hook, kg; *y*: Any distance from the neutral axis along the width (*W*), mm; P_o: Maximum contact load per unit length, N/mm; a_1, b_1: Major and Minor axis of the Hertzian contact ellipse, mm; m_1, n_1: Functions of the geometry of the contact surfaces; R_1, R_2: Principal radii of relative curvature, mm; Ψ_1: Pressure angle between cam and follower, (°); *α*: Angle between the planes containing curvatures $\frac{1}{R_1}$ and $\frac{1}{R_2}$, (°); R_b: Radius of the base circle, m; $M_r, M_\theta, M_{r\theta}$: Circular bending and twisting moments, N·mm; ρ: Pear cam density, kg/m^3; *D*: Bending rigidity, N·mm; *r*: Radius of curvature at any point on the cam profile, mm; *W*(*r*, Θ, *t*): Bending deflection, mm; ω_n: Natural frequency of the cam, rad/s; *m*: Single trigonometric of infinite series ($m = 1,2,3,...,\infty$); R_P, θ_P: Radius of curvature and angle of contact at the point of contact, mm and (°) respectively; r_1: Hub radius, mm; t_1: Time at any angle of contact (θ_P) excluding the time of the dwell stroke, s; *z*: Variable thickness through the pear cam thickness, mm; $\sigma_r, \sigma_\theta, \sigma_{r\theta}$: Circular bending and twisting stresses, N/mm^2; σ_1, σ_2: Principal stresses, N/mm^2; σ_V: Von Mises stress, N/mm^2.

Acknowledgements

The author is grateful to the strength of material research laboratory at the University of Baghdad for the totally support. The author would also like to thank the referees for their careful reading of the paper and helpful suggestions.

Authors' Contributions

LSY was in charge of the analytic solution, simulation procedure and experiment setup; LSY wrote the whole manuscript; NHH assisted with sampling manufacturing and laboratory test analyses. All authors read and approved the final manuscript.

Authors' Information

Louay Sabah Yousuf was born in Baghdad, Iraq in 1979. He received the B.Sc., M.Sc. and Ph.D. degrees in Mechanical Engineering from *Baghdad University, College of Engineering, Baghdad, Iraq*, in 2001, 2004, and 2008 respectively. Since 2014 to 2016, he was a Research Assistant with Mechanical Impact Laboratory at the *Department of Mechanical Engineering, Auburn University, Alabama, USA* before joining *San Diego State University, USA*. From 2008 till current he is a visiting Assistant Professor at *Department of Mechanical Engineering, San Diego State University, USA*. His research interests include non-linear dynamics

of cam and follower, composite materials, finite element method, vibrations, and experimental stress analysis.

Nabil Hassan Hadi was born in Baghdad, Iraq in 1966. He received the B.Sc. and M.Sc. degrees in Mechanical Engineering from *Baghdad University, College of Engineering, Baghdad, Iraq*, in 1987, 1993. He received his Ph.D. degree from *ST.PETERSBURG POLYTECHNIC University, Federal Republic of Russia*, in 2002. Currently, he is a full professor and head of Aeronautical Department at the *University of Baghdad*. He has 21 papers, 4 conference papers and one patent.

Funding
Not applicable.

Competing Interests
The author declare that they have no conflict of interest.

Author Details
[1] Department of Mechanical Engineering, San Diego State University, 5500 Campanile Drive, San Diego, CA 92182-1323, USA. [2] Aeronautical Engineering Department, College of Engineering, University of Baghdad, Baghdad, Iraq.

Received: 28 January 2020 Revised: 27 December 2020 Accepted: 8 January 2021
Published online: 22 February 2021

References

[1] S Sundar, J T Dreyer, R Singh. Rotational sliding contact dynamics in a non-linear cam-follower system as excited by a periodic motion. *Journal of Sound and Vibration*, 2013, 332(12): 4280-4295.
[2] M Machado, P Moreira, P Flores, et al. Compliant contact force models in multibody dynamics: Evolution of the Hertz contact theory. *Journal of Mechanism and Machine Theory*, 2012, 53:99-121.
[3] J H Kuang, C M Hsu, C C Hu. Dynamic behavior of globoidal cam systems with torque compensation mechanisms. *Journal of Mechanism and Machine Theory*, 2010, 45(8): 1201-1214.
[4] D Y Hua, K Farhang, L E Seitzman. A multi-scale system analysis and verification for improved contact fatigue life cycle of a cam-roller system. *Journal of Tribology*, 2007, 129(2): 321-325.
[5] D F Lahr, D W Hong. Contact stress reduction mechanisms for the cam-based infinitely variable transmission. *Proceedings of the ASME 2007 International Design Engineering Technical Conferences & Computers and Information in Engineering Conference IDETC/CIE 2007*, May 20, 2009: 449–456.
[6] K L Hsu, H A Hsieh. Positive-drive cam mechanisms with a translating follower having dual concave faces. *Journal of Mechanisms and Robotics*, 2016, 8(4): 044504.
[7] B C Fabien, R W Longman, F Freudenstein. The design of high-speed dwell-rise-dwell cams using linear quadratic optimal control theory. *Journal of Mechanical Design*, 1994, 116(3): 867-874.
[8] J Angeles, S K Saha, C S Lo´pez-Caju´n. The design of cam mechanisms with translating flat-face followers under curvature constraints. *Journal of Mechanical Design*, 1994, 116(1): 306-310.
[9] M Chew, F Freudenstein, R W Longman. Application of optimal control theory to the synthesis of high-speed cam-follower systems. Part 2: System optimization. *Journal of Mechanical, Transmission and Automation*, 1983, 105(3): 585-591.
[10] P Flores. A computational approach for cam size optimization of disc cam-follower mechanisms with translating roller followers. *Journal of Mechanisms and Robotics*, 2013, 5(4): 041010.
[11] S F Felszeghy. Steady-state residual vibrations in high-speed, Dwell-type, rotating disk cam-follower systems. *Journal of Vibration and Acoustics*, 2005, 127(1): 12-17.
[12] S S Rao. Analysis and synthesis of mechanical error in cam-follower systems. *Journal of Mechanical Design*, 1982, 104(1): 52-62.
[13] D Planchard. *SOLIDWORKS 2017 Reference Guide*. Pap/Psc edition. USA: SDC Publisher, January 3, 2017.
[14] J E Shigley. *Theory of machines and mechanisms*. 1st ed. New York: Oxford University Press, 2011.
[15] L S Yousuf, D B Marghitu. Non-linear dynamic analysis of a cam with flat-faced follower linkage mechanism. *Proceedings of the ASME 2017 International Mechanical Engineering Congress and Exposition IMECE 2017*, January 10, 2018: V04AT05A051.
[16] R Budynas, K Nisbett. *Shigley's mechanical engineering design*.10th ed. New York: McGraw-Hill Education, 2014.
[17] A H Slocum. *Precision machine design*. Illustrated edition. Southfield, MI: Society of Manufacturing Engineers, 1992.
[18] H Gheadnia, O Cermik, D B Marghitu. Experimental and theoretical analysis of the elasto-plastic oblique impact of a rod with a flat. *International Journal of Impact Engineering*, 2015, 86: 307-317.
[19] G Fei, Y Liu, W H Liao. Cam profile generation for cam-spring mechanism with desired torque. *Journal of Mechanisms and Robotics*, 2018, 10(4): 041009.
[20] J Angeles, L Cajún, S Carlos. *Optimization of cam mechanisms*. 1st ed. Netherlands: Springer, 2012.
[21] J M Thompson, M K Thompson. *ANSYS mechanical APDL for finite element analysis*. 1st ed. Oxford: Butterworth-Heinemann, 2017.
[22] B Bhushan. *Introduction to tribology*. 2nd ed. New Jersey: John Wiley & Sons, 2013.
[23] B Bhushan. *Modern tribology handbook*. 1st ed. Boca Raton: CRC Press, 2001.
[24] E J Hearn. *Mechanics of materials*. 3rd ed. UK: Pergamon Press, 1985.
[25] K Ramesh, G Lewis. Digital photoelasticity: Advanced techniques and applications. *Journal of Applied Mechanics Review*, 2002, 55(4): B69-B71.
[26] R J Lang, T Nelson, S Magleby, et al. Thick rigidly foldable origami mechanisms based on synchronized offset rolling contact elements. *Journal of Mechanisms and Robotics*, 2017, 9(2): 021013.
[27] R Szilard. Theories and applications of plate analysis: classical, numerical, and engineering methods. *Journal of Applied Mechanics Review*, 2004, 57(6): B32-B33.
[28] S P Timoshenko, W K Sergius. *Theory of plates and shells*. 2nd ed. USA: McGraw-Hill College, 1959.
[29] N K Bairagi. *A text book of plate analysis*. 2nd ed. India: Khanna, 1986.